

CPFI-EIT: A CNN-PINN Framework for Full-Inverse Electrical Impedance Tomography on Non-Smooth Conductivity Distributions

Xuanxuan Yang^{1,2}, Yangming Zhang¹, Haofeng Chen^{1,2}, Gang Ma^{*2}, Xiaojie Wang^{*1}

Abstract—This paper introduces a hybrid learning framework that combines convolutional neural networks (CNNs) and physics-informed neural networks (PINNs) to address the challenging problem of full-inverse electrical impedance tomography (EIT). EIT is a noninvasive imaging technique that reconstructs the spatial distribution of internal conductivity based on boundary voltage measurements from injected currents. This method has applications across medical imaging, multiphase flow detection, and tactile sensing. However, solving EIT involves a nonlinear partial differential equation (PDE) derived from Maxwell’s equations, posing significant computational challenges as an ill-posed inverse problem. Existing PINN approaches primarily address semi-inverse EIT, assuming full access to internal potential data, which limits practical applications in realistic, full-inverse scenarios. Our framework employs a forward CNN-based supervised network to map differential boundary voltage measurements to a discrete potential distribution under fixed Neumann-to-Dirichlet (NtD) boundary conditions, while an inverse PINN-based unsupervised network enforces PDE constraints for conductivity reconstruction. Instead of traditional automatic differentiation, we introduce discrete numerical differentiation to bridge the forward and inverse networks, effectively decoupling them, enhancing modularity, and reducing computational demands. We validate our framework under realistic conditions, using a 16-electrode setup and rigorous testing on complex conductivity distributions with sharp boundaries, without Gaussian smoothing. This approach demonstrates robust flexibility and improved applicability in full-inverse EIT, establishing a practical solution for real-world imaging challenges.

Index Terms—Electrical impedance tomography, Convolutional neural networks, Physics-informed neural networks, Computational imaging

I. INTRODUCTION

ELECTRICAL Impedance Tomography (EIT) [1] is a form of tomographic imaging that calculates the spatial distribution of internal conductivity by injecting currents and measuring boundary voltages. EIT has broad applications in fields such as medical imaging [2], multiphase flow detection [3], and tactile sensing [4]. Solving EIT involves a nonlinear partial differential equation (PDE) derived from Maxwell’s equations and presents a computationally challenging, ill-posed inverse problem. Physics-Informed Neural Networks

(PINNs) have recently emerged as a machine learning approach for solving PDEs [5], [6]. By embedding additional physical constraints into the loss function, PINNs approximate PDE solutions by minimizing the physics-informed loss during training. This approach, known as Learning with Physics Loss [7], offers strong interpretability and has demonstrated significant advantages for solving inverse problems [8], [9]. Consequently, researchers have started exploring the use of PINNs to enable tomographic imaging, including applications to EIT [10]–[12].

However, existing research on using PINNs for EIT has primarily focused on the semi-inverse EIT problem [10], [11], where it is assumed that the internal potential field is fully accessible. L. Bar et al. [10] were the first to apply PINNs for semi-inverse EIT, followed by A. Pokkunuru et al. [11], who introduced data-driven energy-based priors [13] to accelerate PINN convergence and improve imaging accuracy. Solving semi-inverse EIT involves two networks: a forward network and an inverse network. The forward PINN network $f_u^{semi}(x, y)$ predicts the potential $u(x, y)$ at any point $(x, y) \in \mathcal{H} \subset \mathbb{R}^2$, given the known conductivity distribution within the target domain \mathcal{H} . The inverse PINN network $f_\sigma^{semi}(x, y)$, on the other hand, estimates the conductivity $\sigma(x, y)$ across \mathcal{H} , given the internal potential field $u(x, y)$ at all points. Automatic differentiation (AD) is then applied to $f_u^{semi}(x, y)$ to compute the gradient, which serves as a constraint in the PDE loss for the inverse network. This approach requires $f_u^{semi}(x, y)$ to be explicitly differentiable, allowing the use of tools like TensorFlow’s *tf.gradients* function. This smoothness assumption [14] underpins the Gaussian-smoothing used in these studies, restricting conductivity distributions to simple shapes, such as circles or ellipses.

But in practice, we often face the full-inverse EIT problem, where only limited boundary voltage measurements are accessible, and the goal is to reconstruct the conductivity distribution in \mathcal{H} . Although more challenging, efforts have been made by L. Bar et al. and A. Pokkunuru et al. in this area. A. Pokkunuru et al. acknowledged that their method could only reconstruct simple shapes (circles or ellipses), and failed when faced with more complex distributions. They also attempted to replicate L. Bar et al.’s approach but were unsuccessful, commenting, “To the best of our knowledge, only Bar & Sochen (2021) claim to train the EIT inverse problem using PINNs by jointly training u -Net and σ -Net, but unfortunately, their implementation is not open-source and we were unable to reproduce their results based on the

Xiaojie Wang (e-mail: xjwang@iamt.ac.cn), Gang Ma (e-mail: magang93@ustc.edu.cn)

¹Xuanxuan Yang, Yangming Zhang, Haofeng Chen and Xiaojie Wang are with the Hefei Institutes of Physical Science, Chinese Academy of Sciences, Hefei 230031, China.

²Xuanxuan Yang, Haofeng Chen and Gang Ma are with the University of Science and Technology of China, Hefei, Anhui 230026, China.

details in the paper.” This suggests that true full-inverse EIT remains unachieved due to the need for simultaneous training of multiple forward networks and a single inverse network, which presents significant convergence challenges.

Given these challenges, the limitations of existing works are as follows:

- 1) Current methods [10], [11] are restricted to the idealized semi-inverse EIT scenario and are not yet capable of addressing full-inverse EIT under realistic conditions.
- 2) To ensure explicit differentiability of the forward network $f_u^{semi}(x, y)$, existing methods rely on the assumption that conductivity is smooth and continuous [14]. This is incompatible with real-world scenarios where conductivity distributions may be discontinuous or exhibit sharp boundaries [15].
- 3) In full-inverse EIT, the boundary conditions vary with each change in excitation source position. When the source position changes K times, joint training of K forward networks and a single inverse network is required. This simultaneous training imposes dependency across all $K+1$ networks in terms of parameters, loss functions, and gradient updates, which strengthens the coupling between forward and inverse networks [7], [10], [11]. Consequently, this approach results in increased computational costs, memory usage, time, and convergence difficulties.

To address the limitations discussed above, we propose a hybrid imaging framework that combines CNN and PINN, decoupling the forward and inverse problems to enable practical application of PINNs in full-inverse EIT. Recently, CNNs have become indispensable in image processing due to their ability to capture spatial features and invariant patterns, demonstrating exceptional performance in tasks such as image segmentation [16], regression [17], and object detection [18]. Observing that potential distributions exhibit spatial characteristics similar to images, we leverage CNNs to capture the relationship between boundary voltage measurements and internal potential distributions. Thus, we construct a data-driven, supervised forward network using CNNs to output a discrete potential distribution \mathcal{U}_d under fixed Neumann-to-Dirichlet (NtD) boundary conditions for any given boundary voltage measurement ΔV . Subsequently, we design a model-driven, unsupervised inverse network using PINNs, which obtains the necessary PDE constraints via discrete numerical differentiation of the forward network’s output \mathcal{U}_d . This enables the reconstruction of the conductivity distribution Σ from the discrete potential field \mathcal{U}_d , effectively bridging the data-driven and physics-driven components of the framework.

The contributions of this paper are as follows:

- 1) We introduce a novel hybrid learning framework to address the limitations of using PINNs for full-inverse EIT—a first, to the best of our knowledge. The forward network provides a potential distribution under fixed NtD boundary conditions, while the inverse network ensures that the final solution satisfies physical laws and boundary conditions.
- 2) We introduce discrete numerical differentiation to bridge

the forward and inverse networks, eliminating the traditional PINN reliance on automatic differentiation and its associated smoothness assumptions for conductivity. By using gradient information obtained through numerical differentiation, the inverse PINN network is guided to satisfy the necessary physical constraints.

- 3) By employing discrete numerical differentiation instead of automatic differentiation, our approach allows the forward network to output a discrete solution. This enables us to design a data-driven, supervised forward network using CNNs, which generates a discrete potential distribution \mathcal{U}_d . This decouples the forward and inverse problems, allowing the forward network to be trained just once to quickly produce the discrete potential field. As a result, we overcome the limitations of traditional PINN methods (TPMs), which require multiple forward networks to accommodate changing boundary conditions.
- 4) Our approach is designed to more closely align with real-world conditions. We replace continuous boundary excitation with a 16-electrode setup, and conduct tests under stricter conditions. This includes avoiding Gaussian smoothing for conductivity fields and testing with objects that feature sharp boundaries, such as triangles and squares. Additionally, we demonstrate full-inverse EIT using real-world data for the first time.

II. MATHEMATICAL ANALYSIS OF PINN-BASED EIT: FROM TPM TO CPFI-EIT

A. PDE-based formulation of EIT

The PDE forms the foundation of PINNs, and we will now use it to provide a clearer description of EIT, which reconstructs the spatial conductivity σ in target domain $\mathcal{H} \subset \mathbb{R}^2$ based on voltage difference measurements by electrodes at the boundary $\partial\mathcal{H}$. The distribution of the potential u within the ROI is governed by an elliptic equation:

$$-\nabla \cdot (\sigma \nabla u) = 0 \quad \text{in } \mathcal{H} \subset \mathbb{R}^2 \quad (1)$$

To initiate the EIT process, a current ζ is applied to the surface $\partial\mathcal{H}$ via electrodes at the boundary, and the resulting voltage $u|_{\partial\mathcal{H}} = \kappa$ on $\partial\mathcal{H}$ is measured. Under these conditions, the Neumann and Dirichlet boundary conditions are defined as:

$$\sigma \left(\frac{\partial u}{\partial n} \right) = \zeta \quad \text{on } \partial\mathcal{H} \quad (2)$$

$$u|_{\partial\mathcal{H}} = \kappa \quad \text{on } \partial\mathcal{H} \quad (3)$$

where n represents the outward unit normal vector on $\partial\mathcal{H}$. Together, these conditions define the Neumann-to-Dirichlet (NtD) operator:

$$\Lambda_\sigma : \zeta \mapsto \kappa \quad (4)$$

where Λ_σ maps the applied current ζ to the measured boundary voltage κ , providing the mathematical basis for reconstructing conductivity σ .

Electrical Impedance Tomography (EIT) reconstructs the spatial conductivity distribution $\sigma(x, y)$ in \mathcal{H} based on boundary voltage measurements $\partial\mathcal{H}$. The mathematical foundation

of EIT lies in solving the PDE described by Equation (1), governed by an elliptic operator with Neumann and Dirichlet boundary conditions. These conditions, defined by the Neumann-to-Dirichlet (NtD) operator, establish the relationship between the applied current ζ and the resulting boundary voltage κ .

However, traditional PINN-based methods (TPM) and our proposed CPFI-EIT differ significantly in their approach to Neumann boundary conditions, conductivity assumptions, and handling of discrete data. Below, we mathematically formalize these differences to highlight the advantages of CPFI-EIT in addressing full-inverse EIT challenges.

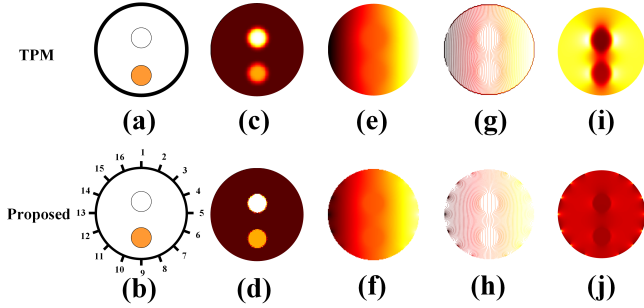


Fig. 1. (a)Continuous excitation on the boundary. (b)Excitation by electrodes on the boundary. (c)Conductivity distribution with Gaussian low-pass filtering. (d)Conductivity distribution without Gaussian low-pass filtering.(e)Electric potential field. (f)Electric potential field. (g)Contour of the electric potential field. (h)Contour of the electric potential field. (i)The partial derivative of the potential distribution with respect to the x -direction. (j)The partial derivative of the potential distribution with respect to the x -direction.

B. Neumann Condition Based on Finite Electrodes

In TPMs, the Neumann boundary condition is set by applying continuous excitation along the entire boundary, as illustrated in Fig. 1(a). This excitation is typically controlled by a trigonometric function [19], which generates a potential field in the internal region upon current injection, shown in Fig. 1(c) with its corresponding contour plot in Fig. 1(d).

While continuous boundary excitation can enhance imaging quality, it is an idealized setup. To evaluate the performance of CPFI-EIT under conditions closer to real-world scenarios, we apply excitation using 16 discrete electrodes along the boundary, as shown in Fig. 1(b). The excitation function is defined as

$$\zeta = \frac{1}{\sqrt{2\pi}} \sin(\omega k + \varphi) \quad (5)$$

where the frequency $\omega = \frac{\pi}{8}$, k represents the electrode index, with $k \in \mathbb{Z}$, $1 \leq k \leq 16$, and the phase $\varphi = 0$. The corresponding potential field and contour plot are shown in Fig. 1(g) and (h), respectively.

C. Non-Smooth Conductivity Assumption

In TPMs, all experiments are conducted under the assumption of smooth conductivity, as shown in Figure 1(b). This is necessary because automatic differentiation requires the forward network $u(x, y) = f_u^{semi}(x, y)$ to be differentiable

in order to compute the PDE loss term in the inverse network $f_\sigma^{semi}(x, y)$. The automatic differentiation (AD) approach is formulated as follows:

$$\mathcal{U} = \{u(x, y) = f_u^{semi}(x, y) \mid (x, y) \in \mathcal{H}\} \quad (6)$$

$$\frac{\partial u}{\partial x} = f^{AD}(u(x, y), x), \quad \frac{\partial u}{\partial y} = f^{AD}(u(x, y), y) \quad (7)$$

where \mathcal{U} represents the continuous potential field, and f^{AD} denotes the automatic differentiation tool, such as TensorFlow's *tf.gradient* function. However, this introduces a limitation: for a unique solution $u(x, y) \in C^2(\mathcal{H})$ to exist, the conductivity distribution must satisfy the

$$0 < l_b \leq \sigma(x, y) \in C^1(\mathcal{H}) \quad (8)$$

which implies that $\sigma(x, y)$ must be strictly positive and continuously differentiable throughout \mathcal{H} [14]. To align more closely with real-world conditions, as illustrated in Figure 1(f), we remove the smooth conductivity assumption, allowing for conductivity distributions that are piecewise continuous rather than globally smooth. In this setting, conductivity can be represented as

$$\sigma(x, y) \in PC(\mathcal{H}) \quad (9)$$

where $PC(\mathcal{H})$ denotes the piecewise continuous function space, with $\sigma(x, y)$ being continuous within each subregion but possibly discontinuous across the boundaries. Additionally, we challenge our framework by reconstructing more complex conductivity shapes, including triangles and squares with sharp boundaries, and, for the first time, incorporating real experimental data.

D. Discrete Numerical Differentiation for Approximating Continuous Fields

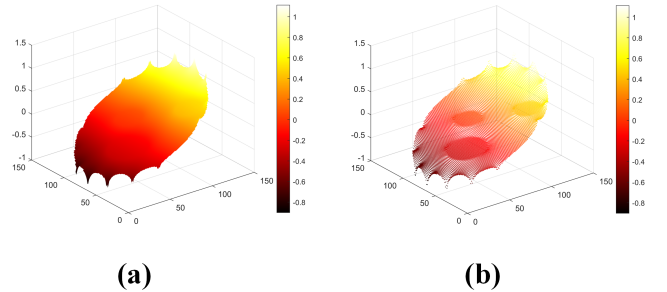


Fig. 2. (a)Continuous potential distribution. (b)Discrete potential distribution.

By employing discrete numerical differentiation, we can approximate gradients without requiring $\sigma(x, y)$ to be smooth. This approach also enables our solution to be defined on a discrete grid, eliminating the need for a continuous, differentiable solution across the entire domain. Fig.2(a) and (b) illustrate the outputs of the forward network in TPM and CPFI-EIT, respectively. Thus, we construct a CNN-based forward network to efficiently predict the discrete potential distribution \mathcal{U}_d over a 128×128 two-dimensional grid $\mathcal{D} \subset \mathbb{Z}^2$, defined as follows:

$$\mathcal{U}_d = \{u_d(x, y) \mid (x, y) \in \mathcal{D}\} \quad (10)$$

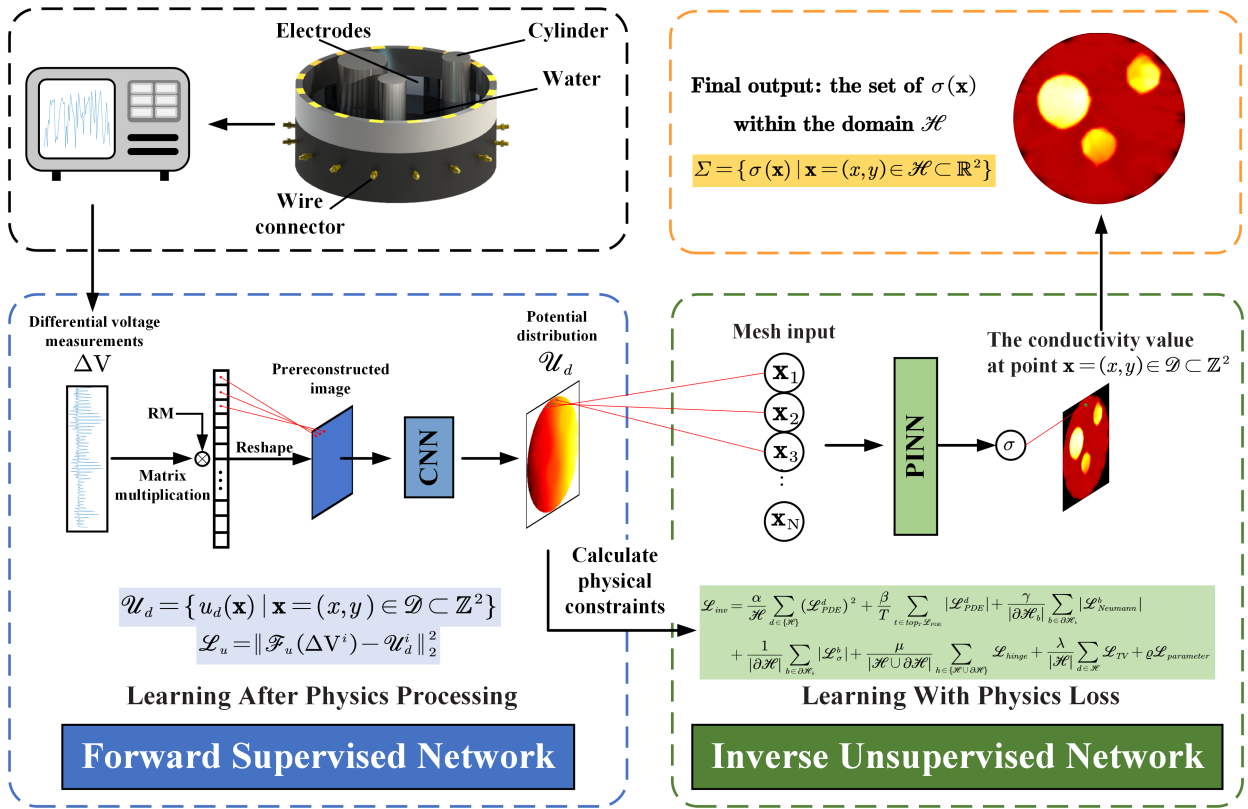


Fig. 3. The architecture of CPFI-EIT algorithm

Next, we apply finite difference approximations on the discrete potential field to obtain numerical gradients at each grid point:

$$\begin{aligned} \frac{\partial u_d}{\partial x} &\approx \frac{u_d(x+1, y) - u_d(x-1, y)}{2h} \\ \frac{\partial u_d}{\partial y} &\approx \frac{u_d(x, y+1) - u_d(x, y-1)}{2h} \end{aligned} \quad (11)$$

where h represents the grid spacing. This framework leverages CNNs to capture spatial dependencies on a discrete grid while preserving flexibility to handle non-smooth conductivity distributions.

E. Semi-inverse EIT and full-inverse EIT

The goal of EIT is to reconstruct the conductivity distribution within the ROI $\mathcal{H} \subset \mathbb{R}^2$:

$$\Sigma = \{\sigma(x, y) \mid (x, y) \in \mathcal{H}\} \quad (12)$$

Compared to the semi-inverse EIT problem, where the conductivity at a given point is reconstructed from the known potential at that point, achieving full-inverse EIT is significantly more challenging. This is because boundary voltage measurements are often far fewer and less informative than internal potential data. The formulations for semi-inverse EIT and full-inverse EIT are as follows:

$$u(x, y) \xrightarrow{TPM} \sigma(x, y) \quad (13)$$

$$\Delta V \xrightarrow{CPFI-EIT} \sigma(x, y) \quad (14)$$

III. METHOD

The overall framework of CPFI-EIT is illustrated in Fig. 3, comprising the EIT data acquisition module and the CPFI-EIT algorithm module. The CPFI-EIT algorithm consists of a forward supervised network \mathcal{F}_u and an inverse unsupervised network \mathcal{F}_σ . First, the EIT data acquisition system collects the boundary voltage measurements ΔV , which are then fed into the forward supervised network \mathcal{F}_u to generate a discrete potential distribution \mathcal{U}_d . Subsequently, discrete numerical differentiation is applied to guide the PDE loss term of the inverse unsupervised network \mathcal{F}_σ , enabling the reconstruction of the conductivity distribution Σ .

A. Forward supervised network

In this section, we provide a detailed introduction to the data-driven supervised forward network \mathcal{F}_u , as illustrated in Fig. 4. The goal of \mathcal{F}_u is to train a mapping from the boundary differential voltage measurements ΔV to the discrete potential distribution \mathcal{U}_d under fixed boundary conditions constrained by Equation (2). This training is performed using the dataset $\{\Delta V^i, \mathcal{U}_d^i\}_{i=1}^N$, and the problem can be formulated as:

$$\hat{\theta} = \arg \max_{\theta} \frac{1}{N} \sum_{i=1}^N \mathcal{L}_u(\mathcal{F}_u(\Delta V^i), \mathcal{U}_d^i) \quad (15)$$

where $\theta = \{W, b\}$ represents the weights and biases of the forward network \mathcal{F}_u , and \mathcal{L}_u is the loss function. Since this is a regression problem, we adopt the mean squared error (MSE) loss, defined as:

Forward Supervised Network

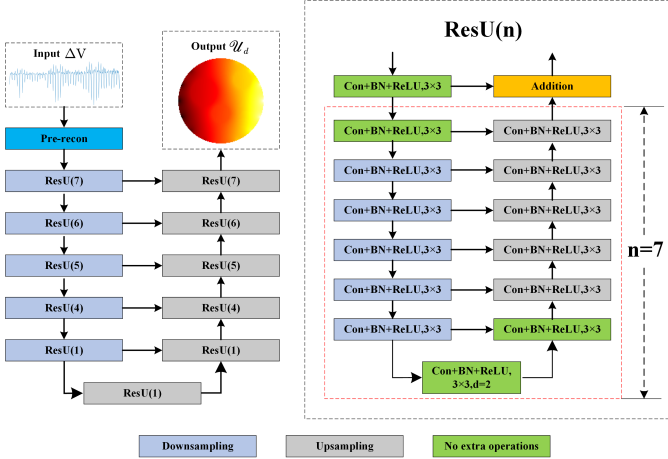


Fig. 4. The architecture of forward supervised network.

$$\mathcal{L}_u(\mathcal{F}_u(\Delta V^i), \mathcal{U}_d^i) = \|\mathcal{F}_u(\Delta V^i) - \mathcal{U}_d^i\|_2^2 \quad (16)$$

1) *Gradient Perspective and Network Design*: When boundary currents are injected, the current experiences abrupt changes as it flows through objects, significantly influencing the potential distribution, as shown in Fig. 1(f). This effect is particularly evident in the spatial gradient of the potential field. As illustrated in Fig. 1(j), applying discrete differentiation in the x -directions reveals patterns that closely resemble the conductivity distribution in form, as shown in Fig. 1(d). This gradient perspective is critical, as it highlights sharp variations in the potential field near object boundaries, enabling the potential changes to be correlated with the underlying conductivity contrasts.

Predicting the discrete potential distribution, however, is inherently challenging due to its far more complex spatial variations compared to conductivity distributions. These variations arise from the interplay of boundary conditions and multiple conductivity regions, making potential distributions visually difficult to interpret or segment. To address this challenge, we experimented with numerous backbone networks [20]–[22], but their performance was suboptimal. This is because most of these networks were originally designed for image classification tasks, focusing on extracting semantically representative features, but falling short in capturing both local details and global contrast information essential for potential distribution prediction.

Ultimately, we drew inspiration from U²-Net [23], a nested U-structured network designed for salient object detection. U²-Net excels at extracting multi-scale contextual information while maintaining resolution, making it particularly well-suited for predicting potential distributions. Our forward network adopts a similar nested architecture but incorporates modifications to tailor it to the unique characteristics of potential fields. Specifically, all convolutional layers in our network utilize 3×3 kernels, and all max-pooling layers employ 2×2 kernels, ensuring consistent spatial scaling and efficient feature

extraction. Additionally, we introduce physics-informed guidance to enhance feature extraction while making the network lightweight and efficient [24]. This modified architecture, shown in Figure 4, effectively balances detail preservation and global context extraction, addressing the unique challenges of potential field prediction.

B. Inverse unsupervised networks

In this section, we introduce the model-driven inverse unsupervised network \mathcal{F}_σ , designed to reconstruct the conductivity distribution $\sigma(x, y)$ within the ROI $\mathcal{H} \subset \mathbb{R}^2$, as shown in Fig. 5. The network takes the coordinates of each point in \mathcal{U}_d as input and uses the discrete numerical gradients of \mathcal{U}_d to enforce PDE constraints, ensuring that the solution $\sigma(x, y)$ converges to a physically valid reconstruction. In addition, the network is inspired by the work of Wang et al. [25], which is a multi-layer perceptron composed of four hidden layers, each of which has 64 neurons and tanh activation function, and residual connections are added to each layer to deepen the network and enhance its performance. Below, we provide a detailed explanation of the loss terms that constitute the inverse PINN network.

1) *PDE constraint loss*: The PDE constraint ensures that the predicted conductivity satisfies the governing physics described by Equation (1). The loss term is defined as:

$$\mathcal{L}_{PDE}^d = \nabla \cdot (\sigma_d \nabla u_d) \quad (17)$$

where \mathcal{L}_{PDE}^d measures the residual of the PDE at point $\mathbf{x} = (x, y) \in \mathcal{H}$. Minimizing this loss term forces \mathcal{F}_σ to produce conductivity values that adhere to the physics of the potential field across the domain \mathcal{H} , thereby reducing global bias and ensuring consistency with the underlying PDE.

2) *Boundary Condition Loss*: To enforce the Neumann boundary conditions from Equation (2), we introduce the following term:

$$\mathcal{L}_{Neumann}^b = \sigma_b \frac{\partial u_b}{\partial n_b} \quad (18)$$

where this term ensures that the predicted conductivity at the boundary satisfies the relationship between the normal derivative of the potential field and the injected current.

Additionally, we incorporate a boundary conductivity loss to further enhance the accuracy and consistency of conductivity predictions at the domain boundaries:

$$\mathcal{L}_\sigma^b = \sigma_b - \sigma_{\partial \mathcal{H}_b}^* \quad (19)$$

where $\sigma_{\partial \mathcal{H}_b}^*$ is the ground truth or expected conductivity values at the boundary. This term constrains the predicted conductivity to align with prior knowledge or experimental data, ensuring that the boundary conditions are consistent with physical expectations.

3) *Regularization loss*: To improve the smoothness, sparsity, and physical realism of the reconstructed conductivity distribution, we introduce several regularization terms. First, the Total Variation (TV) Regularization term [26] is used to promote spatial smoothness in the conductivity distribution

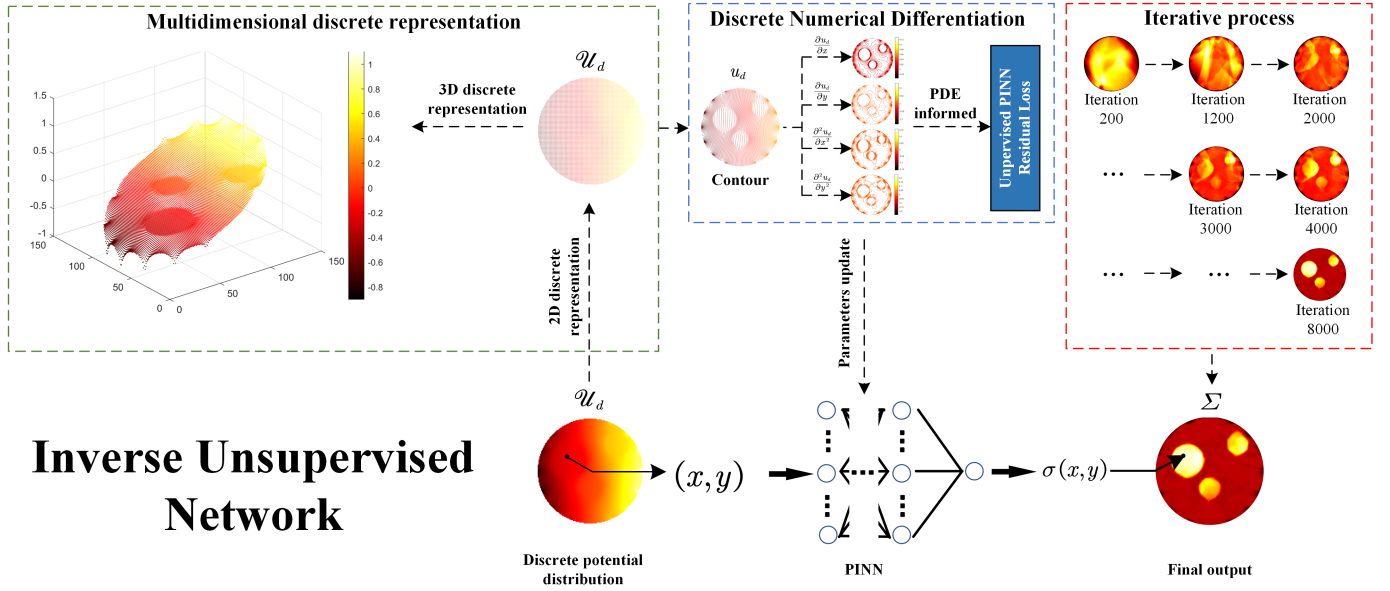


Fig. 5. The architecture of inverse unsupervised network.

and reduce sharp gradients caused by noise or modeling artifacts. It is defined as:

$$\mathcal{L}_{TV} = \sqrt{(\nabla_x \sigma_d)^2 + (\nabla_y \sigma_d)^2} + \xi \quad (20)$$

Additionally, a non-negativity constraint (Hinge Loss) is incorporated to ensure that the predicted conductivity remains physically realistic by enforcing non-negativity:

$$\mathcal{L}_{hinge} = \max(0, 1 - \sigma_h) \quad (21)$$

Finally, a parameter regularization term is introduced to penalize large model weights, thereby preventing overfitting and improving the generalization ability of the network:

$$\mathcal{L}_{parameter} = \|w_\sigma\|^2 \quad (22)$$

which penalizes large model weights, helping to prevent overfitting and improve generalization.

4) *Overall inverse loss*: The final inverse loss function integrates all the individual loss components, weighted by their respective coefficients:

$$\begin{aligned} \mathcal{L}_{inv} = & \frac{\alpha}{|\mathcal{H}|} \sum_{d \in \{\mathcal{H}\}} (\mathcal{L}_{PDE}^d)^2 + \frac{\beta}{T} \sum_{t \in \text{top}T} |\mathcal{L}_{PDE}^d| \\ & + \frac{\gamma}{|\partial \mathcal{H}_b|} \sum_{b \in \partial \mathcal{H}_b} |\mathcal{L}_{Neumann}^b| + \frac{1}{|\partial \mathcal{H}|} \sum_{b \in \partial \mathcal{H}_b} |\mathcal{L}_\sigma^b| \\ & + \frac{\mu}{|\mathcal{H} \cup \partial \mathcal{H}|} \sum_{h \in \{\mathcal{H} \cup \partial \mathcal{H}\}} \mathcal{L}_{hinge} \\ & + \frac{\lambda}{|\mathcal{H}|} \sum_{d \in \mathcal{H}} \mathcal{L}_{TV} \\ & + \varrho \mathcal{L}_{parameter} \end{aligned} \quad (23)$$

Here, the weighting coefficients $\alpha, \beta, \gamma, \lambda, \mu$, and ϱ are hyper-parameters that balance the influence of each loss term.

5) *Hyper-parameters tuning*: The full-inverse EIT problem is highly nonlinear and ill-posed, meaning that even slight changes in parameters can result in dramatic variations in the solution. After extensive testing and optimization, we finalized the hyperparameter settings for our CPFI-EIT framework. To provide a clearer and more intuitive understanding of our hyperparameter choices, we also present a comparison with the hyperparameter settings used in the works of L. Bar et al. and A. Pokkunuru et al., as summarized in Table I. Notably, the hyperparameters δ and ϵ , which are specific electrode-related parameters only used in the works of L. Bar et al. and A. Pokkunuru et al., correspond to values that cannot be directly measured in practice. In our framework, these parameters were optimized to better align with the requirements of real-world applications.

 TABLE I
 COMPARISON OF HYPER-PARAMETERS FOR DIFFERENT METHODS.

Method	Hyper-parameters									
	α	β	T	γ	δ	ϵ	ϱ	λ	μ	ξ
L. Bar et al.	0.01	0.01	40	1	1	1	1e-8	0.01	0	0
A. Pokkunuru et al.	0.05	0.05	40	1	0.1	100	1e-6	0.01	10	0
Ours	0.01	0.01	40	1.5	0	0	1e-6	1	8	1e-4

C. Pseudo code

The pseudo-code of the proposed CPFI-EIT is shown in Algorithm 1.

IV. NUMERICAL AND EXPERIMENTAL STUDIES

This section presents the simulation and real-world experiments conducted to validate the effectiveness of CPFI-EIT for full-inverse EIT. The CPFI-EIT framework was implemented in Python, with the TensorFlow library used to develop

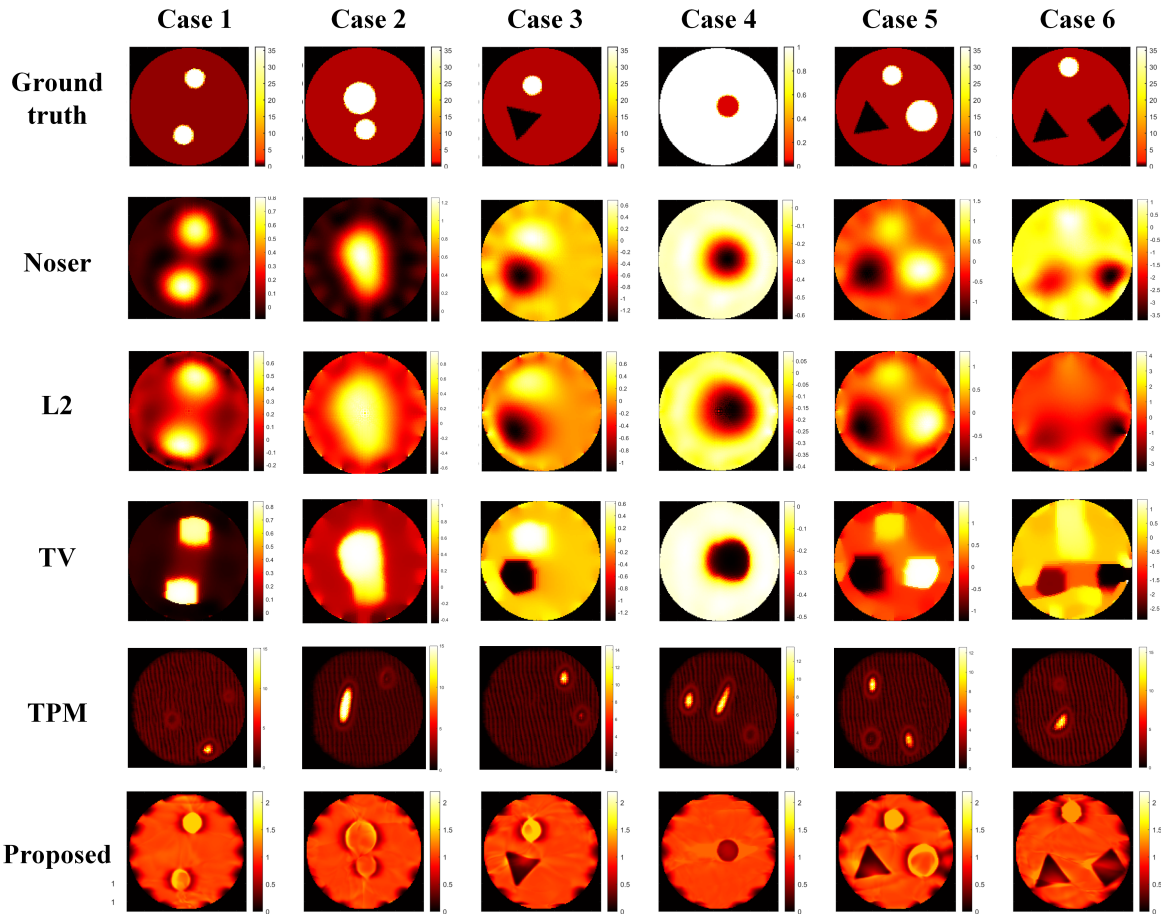


Fig. 6. Full-inverse EIT reconstructions with simulated data.

both the forward and inverse networks. All experiments were performed on a desktop equipped with two NVIDIA GTX 3090 GPUs. To evaluate the performance of CPFI-EIT, we conducted both simulation and experimental tests. Specifically, six simulation cases (cases 1–6, as shown in Fig. 6) were designed, and for the experimental tests, a series of plastic and metal objects with various shapes were placed in a cylindrical tank with a diameter of 28 cm filled with saline water to create diverse conductivity distributions, as illustrated in Fig. 7. The electrodes, current stimulation patterns, and measurement modes in the experimental tests were consistent with those used in the simulations. Experimental data (cases 7–13) [27] were collected using the KIT-4 measurement system [28], further demonstrating the applicability of CPFI-EIT in realistic scenarios.

A. Dataset and training

We utilized EIDORS [29] to generate the dataset for our experiments. A unit circle with a radius of 1 was modeled, incorporating a 16-electrode adjacent measurement pattern. The internal discrete potential distributions were generated under the boundary conditions defined in Equation (2). The finite element mesh consisted of 7744 triangular elements, corresponding to a pixel grid size of 128×128. The dataset included shapes such as circles, equilateral triangles, and

squares, with their positions randomly generated. The dataset categories comprised the following configurations: a single circle, two circles, one equilateral triangle plus one circle, one equilateral triangle plus two circles, and one equilateral triangle combined with one circle and one square. Each category contained 3000 samples. The radii of the circles were randomly generated between 0.1 and 0.28, the side lengths of the equilateral triangles ranged from 0.5 to 0.65, and the squares had side lengths between 0.4 and 0.5. To simulate measurement noise, Gaussian noise with a signal-to-noise ratio (SNR) randomly varying between 40 dB and 60 dB was added to the voltage measurements.

To evaluate CPFI-EIT under extreme conditions, we increased the contrast between the background conductivity and the conductivity of the objects, simulating scenarios such as the presence of metallic objects. This significantly amplified the non-smoothness of the conductivity distribution, with conductivities randomly generated between 0.05 and 36 (excluding the background conductivity of 1). The dataset was split into 80% training data, 10% validation data, and 10% test data.

B. Comparison methods and evaluation indices

To provide a more intuitive demonstration of the effectiveness of CPFI-EIT, we compared our method with three

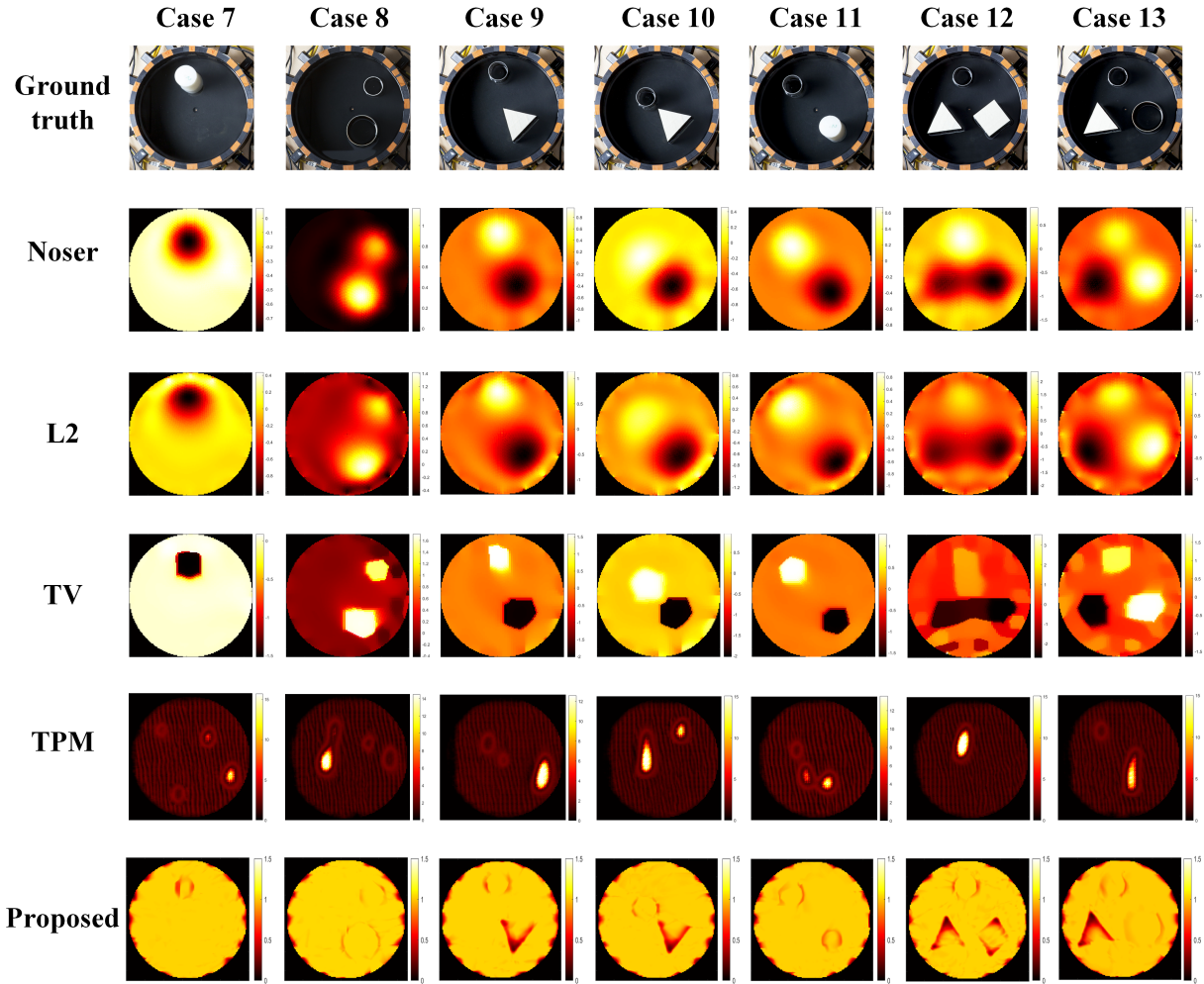


Fig. 7. Full-inverse EIT reconstructions with experimental water tank.

traditional approaches that incorporate different types of prior information: the NOSER prior [30], the Tikhonov prior (L_2 norm prior) [31], and the Total Variation (TV) prior [26]. As discussed in the **Introduction**, the works of L. Bar et al. and A. Pokkunuru et al. were unable to achieve full-inverse EIT under non-smooth conductivity distributions. Consequently, it was not feasible to test their methods in this context for a direct comparison. We also quantitatively evaluated the performance of each method using three metrics: the Structural Similarity Index (SSIM), the Correlation Coefficient (CC), and the Relative Error Index (RIE). A higher SSIM value indicates greater similarity between the reconstructed and true conductivity distributions. The CC measures the linear relationship between the reconstructed and actual conductivity distributions, with a higher CC indicating a closer match. The RIE quantifies the relative error in the reconstruction, where a higher RIE value indicates a larger discrepancy between the reconstructed and true distributions.

C. Simulation results

The reconstruction results using simulation data are shown in Fig. 6. The first row represents the true conductivity distributions, while the second, third, and fourth rows correspond to

the reconstructions using the NOSER, L_2 , and TV algorithms, respectively. The final row displays the results of our proposed CPFI-EIT method. From the comparison of the reconstruction results, it is evident that traditional methods introduce significant artifacts, whereas CPFI-EIT achieves a clear reconstruction of object boundaries and sharp corners, demonstrating its superior performance. Notably, CPFI-EIT also achieves the best evaluation metrics among all methods, as shown in Table II. It is worth highlighting that our approach performs well even under extreme conditions, where the conductivity contrast between the objects and the background is very large (background conductivity = 1, object conductivity = 36). This underscores CPFI-EIT’s ability to handle highly non-smooth conductivity distributions effectively. However, it should be noted that the inverse network in CPFI-EIT is computationally intensive, requiring 7000 to 10,000 iterations for convergence. The primary focus of this work is to address the limitations of L. Bar et al. and A. Pokkunuru et al. in reconstructing non-smooth conductivity distributions and achieving full-inverse EIT. Accelerating the inverse network’s convergence remains an open challenge and will be the focus of our future research.

TABLE II
EVALUATION METRICS FOR CASES 1 TO 6.

Algorithm	Case 1			Case 2			Case 3			Case 4		
	SSIM	CC	RIE	SSIM	CC	RIE	SSIM	CC	RIE	SSIM	CC	RIE
NOSER	0.3369	0.6785	1.0176	0.3919	0.7558	0.5188	0.1897	0.3010	3.6218	0.6246	0.8271	0.2210
L_2	0.2487	0.5512	1.7021	0.2284	0.5308	1.3868	0.1966	0.2779	3.1372	0.5299	0.7624	0.3415
TV	0.3822	0.6752	0.9859	0.2782	0.6713	1.0751	0.2144	0.2985	3.6693	0.6295	0.7709	0.2830
PINN	0.4545	0.7523	0.9675	0.4326	0.7569	0.6935	0.5280	0.5157	2.5022	0.7417	0.9262	0.1455

Algorithm	Case 5			Case 6		
	SSIM	CC	RIE	SSIM	CC	RIE
NOSER	0.2269	0.5172	1.5083	0.1782	0.2596	4.1265
L_2	0.2248	0.5064	1.5190	0.2167	0.2560	2.2984
TV	0.2721	0.5845	1.3841	0.2012	0.2614	3.5919
PINN	0.3551	0.7811	1.0853	0.4193	0.5818	2.2428

TABLE III
EVALUATION METRICS FOR CASES 7 TO 13.

Algorithm	Case 7			Case 8			Case 9			Case 10		
	SSIM	CC	RIE	SSIM	CC	RIE	SSIM	CC	RIE	SSIM	CC	RIE
NOSER	0.6354	0.8351	0.2354	0.4026	0.7654	0.5423	0.1786	0.3159	3.3578	0.1656	0.3650	3.2156
L_2	0.5139	0.7520	0.3546	0.2365	0.5297	1.2693	0.1923	0.2861	3.1355	0.1846	0.2756	3.0362
TV	0.6455	0.7895	0.2642	0.2956	0.6659	1.1123	0.2065	0.2856	3.6494	0.1955	0.2698	3.6038
PINN	0.6312	0.8962	0.2123	0.4287	0.7499	0.7890	0.3956	0.4896	2.8634	0.3731	0.4550	2.9920

Algorithm	Case 11			Case 12			Case 13		
	SSIM	CC	RIE	SSIM	CC	RIE	SSIM	CC	RIE
NOSER	0.3213	0.6697	1.0320	0.1651	0.2687	4.0248	0.2156	0.5023	1.5125
L_2	0.2236	0.5601	1.7009	0.2034	0.2565	2.2652	0.2338	0.5154	1.5003
TV	0.3771	0.6460	0.9623	0.1988	0.2813	3.1365	0.2598	0.5607	1.3512
PINN	0.3811	0.7167	0.9635	0.3985	0.5125	2.2603	0.3645	0.7031	0.9658

D. Experimental results

This section presents the application of CPFI-EIT to achieve full-inverse EIT using real-world physical data, a scenario not previously addressed in TPM. Fig. 7 illustrates the reconstruction results from real-world experiments, where the inclusions consisted of both metal and plastic objects. Similar to the simulation results, traditional methods failed to distinguish the specific shapes of the internal objects, whereas CPFI-EIT successfully reconstructed the shapes and contours of the inclusions with greater clarity. Moreover, CPFI-EIT demonstrated the ability to differentiate between metallic and plastic inclusions. For example, darker colors in the reconstruction represent plastic, while lighter colors indicate metal. It is worth noting that, due to the noise present in real voltage data, the reconstruction quality of CPFI-EIT in real-world experiments is slightly inferior to that in simulations. However, this is expected. Despite the noise, CPFI-EIT significantly outperformed traditional algorithms in accurately reconstructing the shapes and positions of inclusions, as evident in Table III.

V. DISCUSSION: OPTIMAL EXCITATION FREQUENCY STUDY, ROBUSTNESS STUDIES, AND MEDICAL IMAGING APPLICATION

A. Impact of current frequency

To investigate the optimal Neumann boundary conditions, we varied the current frequency applied to the electrodes and

analyzed the corresponding potential and current distributions within the field at different frequencies. Using the inverse network of CPFI-EIT, we performed imaging as shown in Fig. 8. It is clearly observed that as the current frequency increases, the penetration of the current decreases, leading to a deterioration in the imaging performance. This is because, in CPFI-EIT, the inverse network’s loss function is constrained by the physical relationship between the conductivity and the potential distribution. When the current fails to penetrate deeply into the object, the amount of useful information available from the internal potential distribution is reduced, making it more difficult for the network to accurately reconstruct the conductivity distribution. This results in a decrease in the reconstruction accuracy of CPFI-EIT.

B. Robustness studies

To visually demonstrate the noise resilience of CPFI-EIT, we randomly selected a voltage measurement dataset and added Gaussian noise to it, achieving PSNR values of 20dB, 40dB, and 60dB. The resulting noisy data was used for image reconstruction using CPFI-EIT, and evaluation metrics were computed, as shown in Fig. 9. As observed, the reconstructed images remained almost unaffected as the PSNR decreased, indicating the excellent noise robustness of CPFI-EIT. Moreover, our real-world experiments also serve as a robustness analysis,

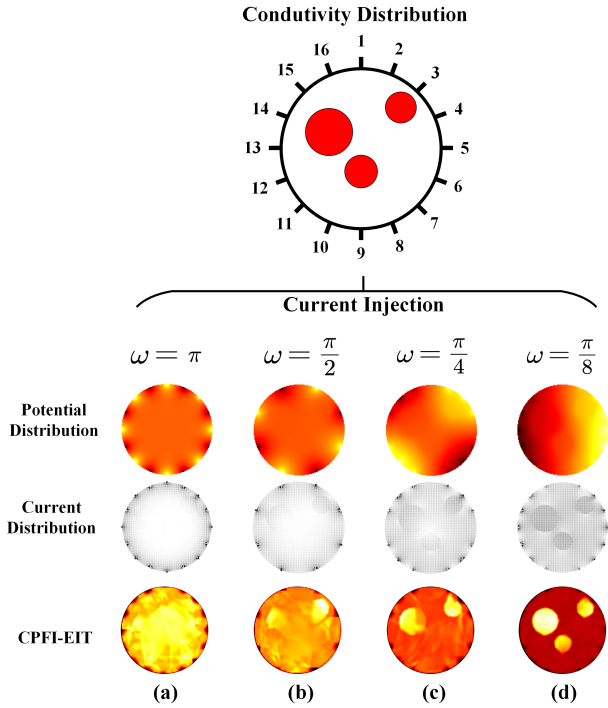


Fig. 8. The internal potential distribution, current distribution, and CPFI-EIT reconstruction results under different Neumann boundary conditions.

as the KIT4 data acquisition system used in the experiments inherently introduces noise into the measurements.

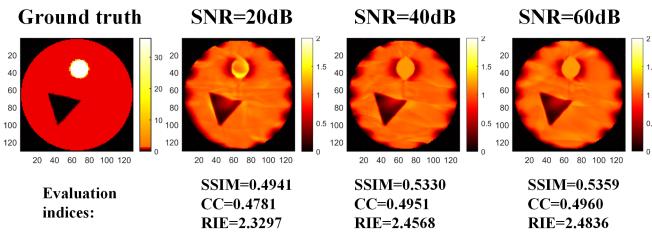


Fig. 9. CPFI-EIT reconstruction results under different noise levels.

C. Application in medical imaging

Medical imaging is a common application of EIT, and in the human body, the conductivity distribution of organs is typically non-smooth, which poses significant limitations for traditional methods such as TPM. To explore the potential of CPFI-EIT in medical imaging, we present an example where lung and heart models made of agar are placed in a circular container filled with physiological saline [32], as shown in Fig. 10(a). We then create the ground truth based on the true model scale and conductivity ratio, as shown in Fig. 10(b), where the conductivity distribution remains non-smooth. In this experiment, we apply the Neumann boundary conditions defined in Equation (5) and use the inverse network of CPFI-EIT for imaging. Additionally, we provide comparative results from three traditional imaging algorithms. From the reconstruction results, it is evident that CPFI-EIT produces clearer

contours compared to the traditional methods, demonstrating its promising potential for medical imaging applications.

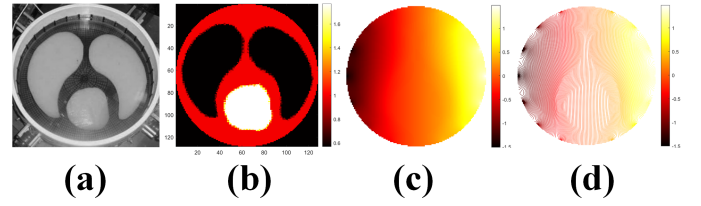


Fig. 10. (a) Medical model of lungs and heart made with agar. (b) Conductivity distribution of (a) based on realistic conductivity ratios. (c) Potential distribution generated under the given Neumann boundary conditions. (d) Contour map corresponding to the potential distribution.

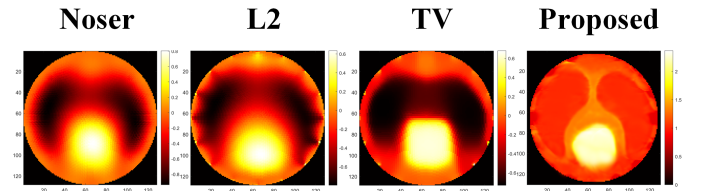


Fig. 11. Simulation results for the network.

Algorithm 1 CPFI-EIT Framework

Require: Training dataset $\{(\Delta V^i, \mathcal{U}_d^i)\}_{i=1}^N$, boundary conditions ζ , loss coefficients $\alpha, \beta, \gamma, \lambda, \mu, \varrho$, grid step size h
Ensure: Reconstructed conductivity distribution $\Sigma = \{\sigma(x, y) \mid (x, y) \in \mathcal{H}\}$

- 1: **Stage 1: Forward Supervised Network**
- 2: Define forward network \mathcal{F}_u parameterized by $\theta = \{W, b\}$
- 3: Train \mathcal{F}_u to minimize the supervised loss:

$$\hat{\theta} = \arg \min_{\theta} \frac{1}{N} \sum_{i=1}^N \|\mathcal{F}_u(\Delta V^i) - \mathcal{U}_d^i\|_2^2$$

- 4: Output discrete potential field $\mathcal{U}_d = \mathcal{F}_u(\Delta V)$
- 5: **Stage 2: Numerical Differentiation on \mathcal{U}_d**
- 6: Compute discrete gradients: $\frac{\partial u_d}{\partial x}, \frac{\partial u_d}{\partial y}$
- 7: **Stage 3: Inverse Unsupervised Network**
- 8: Define inverse network \mathcal{F}_σ parameterized by $\phi = \{w_\sigma\}$
- 9: Initialize ϕ randomly
- 10: Define inverse loss \mathcal{L}_{inv}
- 11: Train \mathcal{F}_σ to minimize \mathcal{L}_{inv}
- 12: **while** not converged **do**
- 13: Update ϕ using gradient descent:

$$\phi \leftarrow \phi - \eta \nabla_{\phi} \mathcal{L}_{inv}$$

- 14: **end while**
- 15: Output reconstructed conductivity distribution:

$$\Sigma = \{\sigma(x, y) \mid (x, y) \in \mathcal{H}\}$$

VI. CONCLUSION

In this paper, we proposed CPFI-EIT, a hybrid learning framework combining CNN and PINN to address the challenges of full-inverse electrical impedance tomography (EIT).

TABLE IV
COMPARISON OF DIFFERENT METHODS.

Method	Work				
	Semi-inverse EIT	Full-inverse EIT	Simulation	Experiment	Non-smooth conductivity distributions
L. Bar et al.	Yes	Yes(They claimed)	Yes	No	No
A. Pokkunuru et al.	Yes	No	Yes	No	No
Ours	Yes	Yes	Yes	Yes	Yes

Our method decouples the forward and inverse problems, overcoming the limitations of traditional PINN frameworks that rely on smooth conductivity assumptions and struggle with full-inverse EIT under non-smooth conditions. By replacing automatic differentiation with discrete numerical differentiation, CPFI-EIT effectively handles real-world scenarios involving sharp boundaries and highly non-smooth conductivity distributions. The forward CNN network in CPFI-EIT accurately predicts discrete potential distributions, capturing intricate spatial variations even under extreme conductivity contrasts, while the inverse PINN network ensures physically plausible conductivity reconstructions by adhering to the underlying PDE constraints. The method demonstrated strong robustness to noise, maintaining high-quality reconstructions even at low signal-to-noise ratios, and outperformed traditional algorithms, such as NOSER, Tikhonov, and TV priors, in both simulated and real-world experiments. CPFI-EIT was successfully applied to full-inverse EIT in real-world scenarios for the first time, clearly reconstructing the shapes and contours of inclusions and distinguishing between metallic and plastic materials. Despite the computational intensity of the inverse network, which requires multiple iterations for convergence, CPFI-EIT's promising performance opens the door for further optimization, and its robustness and scalability make it suitable for a wide range of practical applications. Future work will focus on accelerating the reconstruction process and expanding the framework to address more complex real-world challenges.

ACKNOWLEDGMENTS

This should be a simple paragraph before the References to thank those individuals and institutions who have supported your work on this article.

REFERENCES

- [1] M. Cheney, D. Isaacson, and J. C. Newell, "Electrical impedance tomography," *SIAM review*, vol. 41, no. 1, pp. 85–101, 1999.
- [2] M. Bodenstern, M. David, and K. Markstaller, "Principles of electrical impedance tomography and its clinical application," *Critical care medicine*, vol. 37, no. 2, pp. 713–724, 2009.
- [3] X. Yang, H. Chen, G. Ma, and X. Wang, "Real-time monitoring multiphase flow using electrical impedance tomography," in *2022 IEEE International Conference on Sensing, Diagnostics, Prognostics, and Control (SDPC)*, 2022, pp. 306–311.
- [4] T. Thurner, J. Maier, M. Kaltenbrunner, and A. Schrepf, "Dynamic tactile synthetic tissue: from soft robotics to hybrid surgical simulators," *Advanced Intelligent Systems*, p. 2400199, 2024.
- [5] M. Raissi, P. Perdikaris, and G. E. Karniadakis, "Physics-informed neural networks: A deep learning framework for solving forward and inverse problems involving nonlinear partial differential equations," *Journal of Computational physics*, vol. 378, pp. 686–707, 2019.
- [6] S. Cuomo, V. S. Di Cola, F. Giampaolo, G. Rozza, M. Raissi, and F. Piccialli, "Scientific machine learning through physics-informed neural networks: Where we are and what's next," *Journal of Scientific Computing*, vol. 92, no. 3, p. 88, 2022.
- [7] R. Guo, T. Huang, M. Li, H. Zhang, and Y. C. Eldar, "Physics-embedded machine learning for electromagnetic data imaging: Examining three types of data-driven imaging methods," *IEEE Signal Processing Magazine*, vol. 40, no. 2, pp. 18–31, 2023.
- [8] S. Mishra and R. Molinaro, "Estimates on the generalization error of physics-informed neural networks for approximating a class of inverse problems for pdes," *IMA Journal of Numerical Analysis*, vol. 42, no. 2, pp. 981–1022, 2022.
- [9] M. Baldan, P. Di Barba, and D. A. Lowther, "Physics-informed neural networks for inverse electromagnetic problems," *IEEE Transactions on Magnetics*, vol. 59, no. 5, pp. 1–5, 2023.
- [10] L. Bar and N. Sochen, "Strong solutions for pde-based tomography by unsupervised learning," *SIAM Journal on Imaging Sciences*, vol. 14, no. 1, pp. 128–155, 2021.
- [11] A. Pokkunuru, P. Rooshenas, T. Strauss, A. Abhishek, and T. Khan, "Improved training of physics-informed neural networks using energy-based priors: a study on electrical impedance tomography," in *The Eleventh International Conference on Learning Representations*, 2023.
- [12] G. Ruan, Z. Wang, C. Liu, L. Xia, H. Wang, L. Qi, and W. Chen, "Magnetic resonance electrical properties tomography based on modified physics-informed neural network and multiconstraints," *IEEE Transactions on Medical Imaging*, 2024.
- [13] Y. LeCun, S. Chopra, R. Hadsell, M. Ranzato, F. Huang et al., "A tutorial on energy-based learning," *Predicting structured data*, vol. 1, no. 0, 2006.
- [14] L. C. Evans, *Partial Differential Equations*. American Mathematical Soc., 2010, vol. 19.
- [15] B. M. Graham, *Enhancements in electrical impedance tomography (EIT) image reconstruction for 3D lung imaging*. Citeseer, 2007.
- [16] M. Z. Alom, M. Hasan, C. Yakopcic, T. M. Taha, and V. K. Asari, "Recurrent residual convolutional neural network based on u-net (r2unet) for medical image segmentation," *arXiv preprint arXiv:1802.06955*, 2018.
- [17] N. Kolotouros, G. Pavlakos, and K. Daniilidis, "Convolutional mesh regression for single-image human shape reconstruction," in *Proceedings of the IEEE/CVF conference on computer vision and pattern recognition*, 2019, pp. 4501–4510.
- [18] S. Gidaris and N. Komodakis, "Object detection via a multi-region and semantic segmentation-aware cnn model," in *Proceedings of the IEEE international conference on computer vision*, 2015, pp. 1134–1142.
- [19] S. Siltanen, J. Mueller, and D. Isaacson, "An implementation of the reconstruction algorithm of a nachman for the 2d inverse conductivity problem," *Inverse Problems*, vol. 16, no. 3, p. 681, 2000.
- [20] A. Krizhevsky, I. Sutskever, and G. E. Hinton, "Imagenet classification with deep convolutional neural networks," in *Advances in Neural Information Processing Systems*, F. Pereira, C. Burges, L. Bottou, and K. Weinberger, Eds., vol. 25. Curran Associates, Inc., 2012.
- [21] K. He, X. Zhang, S. Ren, and J. Sun, "Deep residual learning for image recognition," in *Proceedings of the IEEE conference on computer vision and pattern recognition*, 2016, pp. 770–778.
- [22] S. Woo, J. Park, J.-Y. Lee, and I. S. Kweon, "Cbam: Convolutional block attention module," in *Proceedings of the European conference on computer vision (ECCV)*, 2018, pp. 3–19.
- [23] X. Qin, Z. Zhang, C. Huang, M. Dehghan, O. R. Zaiane, and M. Jagersand, "U2-net: Going deeper with nested u-structure for salient object detection," *Pattern recognition*, vol. 106, p. 107404, 2020.
- [24] H. Chen, X. Yang, G. Ma, Y. Wang, and X. Wang, "Enhancing tactile sensing in robotics: Dual-modal force and shape perception with eibased sensors and mm-cnn," in *2024 IEEE International Conference on Robotics and Automation (ICRA)*. IEEE, 2024, pp. 3311–3317.

- [25] S. Wang, Y. Teng, and P. Perdikaris, “Understanding and mitigating gradient flow pathologies in physics-informed neural networks,” *SIAM Journal on Scientific Computing*, vol. 43, no. 5, pp. A3055–A3081, 2021.
- [26] G. González, V. Kolehmainen, and A. Seppänen, “Isotropic and anisotropic total variation regularization in electrical impedance tomography,” *Computers & Mathematics with Applications*, vol. 74, no. 3, pp. 564–576, 2017.
- [27] A. Hauptmann, V. Kolehmainen, N. M. Mach, T. Savolainen, A. Seppänen, and S. Siltanen, “Open 2d electrical impedance tomography data archive,” *arXiv preprint arXiv:1704.01178*, 2017.
- [28] J. Kourunen, T. Savolainen, A. Lehtikoinen, M. Vauhkonen, and L. Heikkinen, “Suitability of a pxi platform for an electrical impedance tomography system,” *Measurement Science and Technology*, vol. 20, no. 1, p. 015503, 2008.
- [29] A. Adler and W. R. Lionheart, “Uses and abuses of eiders: an extensible software base for eit,” *Physiological measurement*, vol. 27, no. 5, p. S25, 2006.
- [30] M. Cheney, D. Isaacson, J. C. Newell, S. Simske, and J. Goble, “Noser: An algorithm for solving the inverse conductivity problem,” *International Journal of Imaging systems and technology*, vol. 2, no. 2, pp. 66–75, 1990.
- [31] M. Vauhkonen, D. Vadász, P. A. Karjalainen, E. Somersalo, and J. P. Kaipio, “Tikhonov regularization and prior information in electrical impedance tomography,” *IEEE transactions on medical imaging*, vol. 17, no. 2, pp. 285–293, 1998.
- [32] D. Isaacson, J. L. Mueller, J. C. Newell, and S. Siltanen, “Reconstructions of chest phantoms by the d-bar method for electrical impedance tomography,” *IEEE Transactions on medical imaging*, vol. 23, no. 7, pp. 821–828, 2004.